JACS
JOURNAL OF THE AMERICAN CHEMICAL SOCIETY
Communication
pubs.acs.org/JACS

Probing the Active Surface Sites for CO Reduction on Oxide-Derived Copper Electrocatalysts

Arnau Verdaguer-Casadevall,[†,⊥] Christina W. Li,[‡,⊥] Tobias P. Johansson,[†] Soren B. Scott,[†] Joseph T. McKeown,[§] Mukul Kumar,[∥] Ifan E. L. Stephens,[†] Matthew W. Kanan,*[,‡] and Ib Chorkendorff*[,†]

[†]Center for Individual Nanoparticle Functionality, Department of Physics, Technical University of Denmark (DTU), Kongens Lyngby, Denmark

[‡]Department of Chemistry, Stanford University, Stanford, California 94305, United States

[§]Materials Science Division, Lawrence Livermore National Laboratory, Livermore, California 94550, United States

[∥]Materials Engineering Division, Lawrence Livermore National Laboratory, Livermore, California 94550, United States

Supporting Information

ABSTRACT: CO electroreduction activity on oxide-derived Cu (OD-Cu) was found to correlate with metastable surface features that bind CO strongly. OD-Cu electrodes prepared by H_2 reduction of Cu_2O precursors reduce CO to acetate and ethanol with nearly 50% Faradaic efficiency at moderate overpotential. Temperature-programmed desorption of CO on OD-Cu revealed the presence of surface sites with strong CO binding that are distinct from the terraces and stepped sites found on polycrystalline Cu foil. After annealing at 350 °C, the surface-area corrected current density for CO reduction is 44-fold lower and the Faradaic efficiency is less than 5%. These changes are accompanied by a reduction in the proportion of strong CO binding sites. We propose that the active sites for CO reduction on OD-Cu surfaces are strong CO binding sites that are supported by grain boundaries. Uncovering these sites is a first step toward understanding the surface chemistry necessary for efficient CO electroreduction.

The use of renewable energy to convert CO_2 into chemicals and fuels is an attractive means of mitigating emissions and increasing energy security.[1,2] Electrochemical CO_2 conversion could help achieve this goal by enabling decentralized CO_2 recycling powered by local renewable electricity sources. One strategy for efficient electrochemical CO_2 conversion is to separate the process into two steps: CO_2 reduction to CO, followed by CO reduction to oxygenates and hydrocarbons. Numerous CO_2 reduction catalysts have been reported that may enable practical CO_2 to CO conversion at low temperature.[3−8] Copper is the only catalyst that has shown significant CO reduction activity in aqueous electrolyte.[9,10] However, the overpotential required to drive CO reduction on polycrystalline Cu foil is prohibitively high, which indicates that the low-index terrace and stepped facets that dominate the surface are inefficient catalysts. We recently showed that nanocrystalline Cu prepared via reduction of a Cu_2O precursor, "oxide-derived Cu" (OD-Cu), has unprecedented activity for the reduction of CO to acetate, ethanol, and propanol.[11] Transmission electron microscopy (TEM) revealed that OD-Cu consists of an interconnected network of nanocrystallites with randomly oriented grain boundaries at the crystallite interfaces. Dispersed nanoparticles of comparable dimensions did not show enhanced CO reduction activity. Based on these data, we hypothesized that grain boundaries created the active sites for CO reduction. Insight into the surface chemistry of OD-Cu is vital for developing improved catalysts.

This study examines the impact of OD-Cu microstructure and adsorbate binding thermodynamics on electrocatalytic CO reduction activity. By comparing OD-Cu to thermally annealed derivatives, we show that the CO reduction activity is tied to metastable structural features. Temperature-programmed desorption (TPD) of CO is then used to probe the binding strength of CO on the surfaces of these electrodes.[12] We show that CO reduction activity correlates with the abundance of strong binding sites that are not found on terraces or stepped surfaces. TPD has been used to study catalysts such as $Cu/ZnO/Al_2O_3$ for methanol synthesis[12,13] as well as model surfaces for low-temperature electrocatalysis,[14−16] but to the best of our knowledge this is the first time TPD has been used on nanocrystalline electrocatalysts.

OD-Cu can be prepared by either electrochemical or H_2 reduction of Cu oxide precursors. For this study, H_2 reduction was used to facilitate TPD experiments. OD-Cu samples were synthesized via air oxidation at 500 °C followed by H_2 reduction at 130 °C (herein referred to as OD-Cu−500).[11] Scanning electron microscopy (SEM) showed aggregated particles in a porous morphology. TEM nanodiffraction indicated that the material is composed of irregularly shaped, 100−300 nm grains that are joined by grain boundaries in a dense polycrystalline network (Figure 1a, e). In order to modulate its structure and catalytic activity, OD-Cu−500 electrodes were annealed under N_2 at 200 and 350 °C. Annealing at 200 °C had little effect on the grain size, while annealing at 350 °C resulted in a smoother morphology and significantly increased grain sizes of ∼1 μm (Figure 1b, c, f, g). For comparison, an OD-Cu electrode was prepared by growing the oxide in air at 300 °C for 30 min and

Received: June 15, 2015
Published: July 21, 2015

© 2015 American Chemical Society

DOI: 10.1021/jacs.5b06227
J. Am. Chem. Soc. 2015, 137, 9808−9811

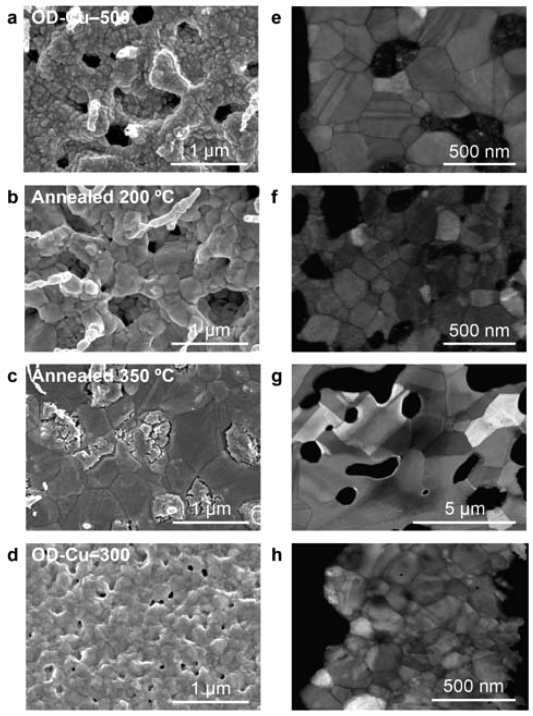

Figure 1. SEM (a–d) and image quality maps constructed from TEM electron diffraction data (e–h) of OD-Cu electrodes. (a, e) OD-Cu–500, (b, f) OD-Cu–500 after 200 °C anneal, (c, g) after 350 °C anneal, (d, h) OD-Cu–300.

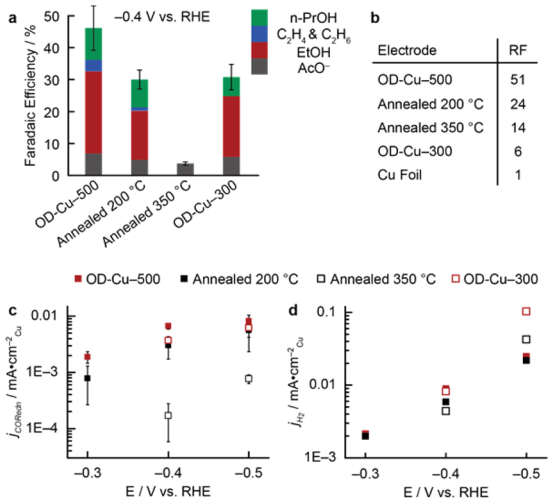

Figure 2. (a) Faradaic efficiency for CO reduction at −0.4 V vs RHE in CO-saturated 0.1 M KOH. The remainder of the charge passed is H_2 evolution. (b) Electrochemical roughness factors (RF). (c) Surface-area corrected j_{CORedn} vs potential. (d) Surface-area corrected j_{H2} vs potential. The error bars represent one standard deviation based on 2–5 measurements.

reducing in H_2 at 130 °C (OD-Cu–300). The grain sizes in OD-Cu–300 are similar to those of OD-Cu–500 and its 200 °C–annealed derivative (Figure 1d, h), but OD-Cu–300 has a much smoother, nonporous morphology, as seen by cross-sectional SEM (Figure S6).

To further characterize the grain boundaries, TEM nanodiffraction was used to collect orientation maps,[17,18] from which grain boundary density and misorientation angles can be extracted. From this analysis, the grain boundary densities of OD-Cu–500, OD-Cu–500 annealed at 200 °C, and OD-Cu–300 are similar: 15 ± 2, 13 ± 1, and 21 ± 2 μm^{-1}, respectively (Figures S9, S10, S11, S13). Moreover, the distribution of grain boundaries is similar in these three electrodes, with ∼37% low-energy twin boundaries and the rest randomly oriented and nontwin coincident site lattice boundaries (Figures S9–S14). By contrast, OD-Cu–500 annealed at 350 °C has a much lower grain boundary density of 1.7 ± 0.1 μm^{-1} with ∼53% twins (Figures S9, S12).

X-ray diffraction and X-ray photoelectron spectroscopy (XPS) of all four samples indicate that the only bulk crystalline phase present is Cu^0, and the surface comprises primarily Cu^0 with some Cu^{1+} due to native oxide formation during transfer of the sample to the XPS chamber (Figures S1–S4). Based on electrochemical capacitance measurements, OD-Cu–500 has a roughness factor of 51 (where electropolished Cu foil is 1) arising from the porous structure. The roughness factor drops to 24 and 14 after annealing at 200 and 350 °C, respectively. OD-Cu–300 has a roughness factor of 6, lower than that of both thermally annealed electrodes.

Electrochemical activity for CO reduction was assessed via constant potential electrolysis in 0.1 M KOH electrolyte under 1 atm CO. As previously reported,[11] OD-Cu–500 exhibits a peak Faradaic efficiency of 48% for CO reduction at −0.4 V vs RHE and generates acetate, ethanol, *n*-propanol, ethylene, and ethane (Figure 2a), measured by gas chromatography and nuclear magnetic resonance (NMR). The surface-area corrected current density for CO reduction (j_{CORedn}) increases with increasing overpotential, but rapidly reaches a plateau corresponding to the mass-transport limit of ∼1 mM dissolved CO in water (Figure 2c).[19]

Upon annealing, the intrinsic CO reduction activity of the electrode is significantly reduced. The surface-area corrected j_{CORedn} is attenuated 2.5-fold on the 200 °C annealed sample and 44-fold on the 350 °C annealed sample (Figure 2c). The loss of intrinsic CO reduction activity is reflected in the Faradaic efficiencies (Figure 2a). The ratios of oxygenate to hydrocarbon products remain similar, but there is a drop in total Faradaic efficiency for CO reduction and a corresponding increase for H_2 evolution. While the 200 °C annealed sample still shows 30% total Faradaic efficiency for CO reduction, the 350 °C annealed electrode has less than 5% efficiency, which is comparable to what was seen previously with commercial Cu nanoparticles.[11] These results suggest that the catalytically active sites are tied to metastable structural features that are kinetically trapped during reduction of the Cu_2O precursor. In contrast, annealing has little effect on the surface area–corrected current density for H_2 evolution (j_{H_2}) (Figure 2d).

The catalytic activity of OD-Cu depends on the thickness of the Cu_2O precursor. OD-Cu–300 is prepared from a thinner oxide than OD-Cu–500, and it has essentially the same surface-area corrected j_{CORedn} and Faradaic efficiency as OD-Cu–500 after annealing at 200 °C. Since OD-Cu–300 has 4-fold lower roughness factor than the 200 °C annealed electrode, this result indicates that neither electrode porosity nor surface area is a significant determinant of CO reduction activity. This conclusion is further supported by the fact that OD-Cu–300 has lower surface area but much higher CO reduction activity than the 350 °C annealed sample.

In order to connect catalytic activity to the thermodynamics of adsorbate binding on the surface, CO-TPD was used to probe the surface chemistry of OD-Cu. To prepare OD-Cu samples for

DOI: 10.1021/jacs.5b06227
J. Am. Chem. Soc. 2015, 137, 9808–9811

TPD, Cu foil was oxidized externally and mounted in the UHV chamber. Adventitious contamination from exposure to air was removed by mildly sputtering the surface, and the samples were reduced at 130 °C under a flow of 1 bar of H_2 (Supporting Information (SI)). XPS at this stage showed a Cu^0 surface (Figure S17) with no trace of Ni (a common contaminant in UHV in the presence of CO due to the formation of nickel carbonyl in the gas lines[20]) or other metallic impurities. The samples were cooled to 77 K, and CO was dosed into the chamber. The temperature was then ramped up at 2 K s^{-1}, and a mass spectrometer monitored the signal from CO at mass 28. The annealed OD-Cu−500 samples were prepared in an identical manner and annealed in UHV prior to CO dosing. The experiments were carried out with a constant dosage of 200 L, which results in variable CO coverage given the different surfaces areas of the samples (Figure S15).

Figure 3a shows a typical TPD profile for electropolished polycrystalline Cu foil. Based on literature data from single crystalline Cu,[12,21,22] the low temperature desorption feature between 100 and 200 K is due to low-index facets such as Cu(111) and Cu(100), and the high temperature feature between 200 and 250 K is characteristic of stepped surfaces such as Cu(211). Figure 3b shows the CO-TPD profile of OD-Cu−500. The OD-Cu−500 profile shows a high-temperature feature centered at 275 K that is clearly absent from the profile for polycrystalline Cu but is present in different proportions in the profiles for the other OD-Cu samples (Figure 3b−e). Annealing OD-Cu−500 to 200 and 350 °C reduces the area of the high-temperature feature (Figure 3c−d). The profile of OD-Cu−300 exhibits broader and less-defined peaks than OD-Cu−500 because its low roughness factor results in a higher CO coverage. Nonetheless, the high-temperature feature is clearly still present on OD-Cu−300 (Figure 3e).

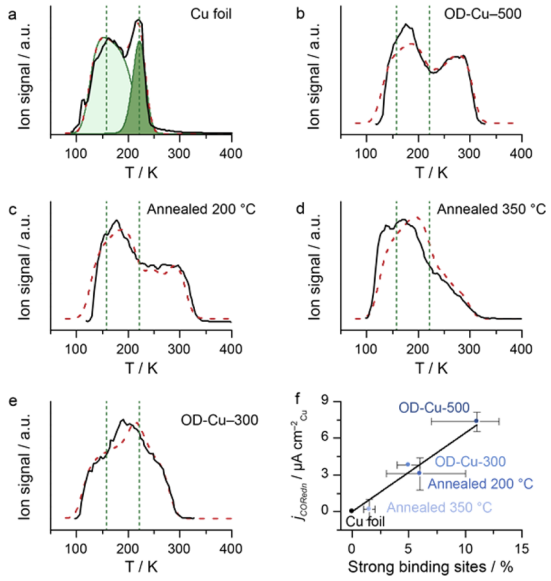

Figure 3. TPD profiles. (a−e) Experimental data (solid black lines) and fit resulting from microkinetic simulations (dashed red lines). The dotted green lines indicate the central position of the low-index facets and stepped sites in polycrystalline Cu. (a) Polycrystalline Cu. Features arising from low-index facets are highlighted in light green, stepped sites are highlighted in dark green; (b) OD-Cu−500; (c) OD-Cu−500 annealed at 200 °C; (d) OD-Cu−500 annealed at 350 °C; (e) OD-Cu−300; (f) Surface-area corrected j_{CORedn} at −0.4 V (vs RHE) vs the percentage of strong binding sites estimated from microkinetic modeling. The solid black line is a linear fit through all of the points. The horizontal error bars are a means of showing the uncertainty in the simulations (described in the SI).

Two possible factors could account for the high-temperature feature in the OD-Cu profiles: (i) CO readsorption in the catalyst layer, which causes peak broadening and a shift of the peak maximum to higher temperature, or (ii) surface sites with enhanced binding to CO. Both of these effects have been observed in TPD studies on industrial $Cu/ZnO/Al_2O_3$ and Cu/SiO_2 catalysts.[23,24] OD-Cu−500 has a large roughness factor, and a significant fraction of the sample surface may reside in mesopores where readsorption could occur. Yet, OD-Cu−300 has the lowest roughness factor of the OD-Cu samples and appears nonporous. Despite its lower roughness factor, OD-Cu−300 presents a higher proportion of the high-temperature feature than the 350 °C annealed sample, indicating that readsorption alone cannot account for the high-temperature feature on OD-Cu.

Direct, quantitative interpretation of the TPD profiles shown here is not possible because the morphology of each sample is different. The same CO dosage gives variations in surface coverage and differing degrees of readsorption on each sample, both of which affect the relative proportions of the low-index, stepped, and strong-binding TPD features. To decouple these effects, the TPD profiles were simulated using microkinetic modeling of CO binding to Cu surfaces with different binding sites and porosities (Figure 3a−e, red dashed line).

To determine the contribution of readsorption to the OD-Cu profiles, simulations were performed for porous polycrystalline Cu with two binding sites that have adsorption energies of ∼52 and ∼60 kJ/mol, which correspond to low-index and stepped facets of Cu (described in the SI). As shown in Figure S21, increasing the depth of the porous layer causes a shift of the TPD profile to higher temperature. While simulated porous polycrystalline Cu has a major peak at 260 K, the overall profile clearly does not fit that of OD-Cu. It is only possible to model the experimental TPD profile for OD-Cu by including a strong binding site with an adsorption energy of ∼67 kJ/mol.

The microkinetic model also enabled quantification of the proportions of each surface site on OD-Cu. OD-Cu−500 has the largest proportion of strong-binding sites with 11% surface coverage. The proportion drops to 5% after annealing at 200 °C and 1.5% after annealing at 350 °C. While these percentages have large uncertainty due to assumptions made about the electrode pore structure, the proportion of strong-binding sites is clearly reduced by thermal annealing. The proportion of strong-binding sites on OD-Cu−300 is 5%. When plotted against electrochemical activity, a linear correlation is obtained between surface area-corrected j_{CORedn} and the percentage of strong binding sites (Figure 3f). On the basis of this correlation, we propose that the active sites for CO reduction at low overpotential on Cu are strong-binding sites. Strong CO binding may increase the rate of CO reduction at a surface site by increasing its steady-state CO coverage. In addition, a high density of strong binding sites at a surface region created by a bulk defect may be necessary if the rate-limiting step involves reductive CO coupling.[25,26] However, these strong-binding sites may not be sufficient for CO reduction. The OD-Cu−500 electrode annealed at 350 °C retains 1.5% of the strong binding site despite having j_{CORedn} that is 44-fold lower than OD-Cu−500. The broad high-temperature feature observed in TPD does not reflect a single surface atomic structure; rather it most likely consists of a range of strained or

DOI: 10.1021/jacs.5b06227
J. Am. Chem. Soc. 2015, 137, 9808−9811

defective structures, all of which bind CO more strongly within an ~10 kJ/mol range. As such, it is possible that only a small subset of these defective structures is capable of catalyzing the CO reduction reaction. In addition, CO is simply a probe molecule in these experiments. In electrolyte solution with an applied potential, the relevant catalytic transition state structures and binding energies may not scale with the CO binding energy in UHV.

The reduction in the proportion of strong binding sites upon thermal annealing qualitatively correlates to the microstructural change observed in TEM. The 7-fold drop in the strong binding sites percentage is similar to the 9-fold drop in grain boundary density observed between OD-Cu-500 and the electrode after 350 °C annealing. Notably, the proportion of strong binding sites estimated from TPD is significantly larger than the proportion of grain boundary surface terminations estimated from TEM. Based on the grain boundary orientation maps and assuming a 1 nm boundary width, we estimate that OD-Cu-500 has 1−2% coverage of grain boundary surface termination area while the TPD modeling indicates 7−15% coverage of strong binding sites. If the grain boundaries are responsible for creating all of the strong binding sites, these results indicate that the surface terminations affect the structure and binding properties of a region that encompasses a much larger width of 4−10 nm. Previous simulations of nanocrystalline fcc metals have shown that grain boundaries strain the surfaces up to several nanometers away.[27] Annealing the samples to a moderate temperature (200 °C) may relax out some of the strong binding sites without significantly changing the grain boundaries.

In summary, we present evidence that the high CO reduction activity on OD-Cu is correlated to surface sites that bind CO more strongly than low-index and stepped Cu facets. These metastable sites may arise from disordered surfaces at grain boundary and defect terminations, which are stabilized by the interconnected nanocrystalline network. Further structural elucidation of the surface of OD-Cu will enable the design and synthesis of more efficient CO reduction catalysts.

■ ASSOCIATED CONTENT

Supporting Information

The Supporting Information is available free of charge on the ACS Publications website at DOI: 10.1021/jacs.5b06227.

Experimental procedures and additional data (PDF)

■ AUTHOR INFORMATION

Corresponding Authors

*mkanan@stanford.edu

*ibchork@fysik.dtu.dk

Author Contributions

⊥A.V.-C. and C.W.L. contributed equally.

Notes

The authors declare no competing financial interest.

■ ACKNOWLEDGMENTS

The Danish National Research Foundation's Center for Individual Nanoparticle Functionality is supported by the Danish National Research Foundation (DNRF54). We thank the Global Climate and Energy Project (106765) and the AFOSR (FA9550-14-1-0132). C.W.L. gratefully acknowledges a Stanford Graduate Fellowship. Sample characterization was performed at the Stanford Nano Shared Facilities. Lawrence Livermore National Laboratory is under the auspices of the U.S. Department of Energy, Contract No. DE-AC52-07NA27344. J.T.M. and M.K. were supported by the Office of Basic Energy Sciences, Division of Materials Science and Engineering under FWP #SCW0939.

■ REFERENCES

(1) Hori, Y. In *Modern Aspects of Electrochemistry*; Vayenas, C. G., White, R. E., Gamboa-Aldeco, M. E., Eds.; Springer: New York, 2008; Vol. *42*, p 89.

(2) Appel, A. M.; Bercaw, J. E.; Bocarsly, A. B.; Dobbek, H.; DuBois, D. L.; Dupuis, M.; Ferry, J. G.; Fujita, E.; Hille, R.; Kenis, P. J. A.; Kerfeld, C. A.; Morris, R. H.; Peden, C. H. F.; Portis, A. R.; Ragsdale, S. W.; Rauchfuss, T. B.; Reek, J. N. H.; Seefeldt, L. C.; Thauer, R. K.; Waldrop, G. L. *Chem. Rev.* **2013**, *113*, 6621.

(3) Chen, Y.; Li, C. W.; Kanan, M. W. *J. Am. Chem. Soc.* **2012**, *134*, 19969.

(4) DiMeglio, J. L.; Rosenthal, J. *J. Am. Chem. Soc.* **2013**, *135*, 8798.

(5) Zhu, W. L.; Michalsky, R.; Metin, O.; Lv, H. F.; Guo, S. J.; Wright, C. J.; Sun, X. L.; Peterson, A. A.; Sun, S. H. *J. Am. Chem. Soc.* **2013**, *135*, 16833.

(6) Mistry, H.; Reske, R.; Zeng, Z. H.; Zhao, Z. J.; Greeley, J.; Strasser, P.; Cuenya, B. R. *J. Am. Chem. Soc.* **2014**, *136*, 16473.

(7) Lu, Q.; Rosen, J.; Zhou, Y.; Hutchings, G. S.; Kimmel, Y. C.; Chen, J. G. G.; Jiao, F. *Nat. Commun.* **2014**, *5*10.1038/ncomms4242.

(8) Asadi, M.; Kumar, B.; Behranginia, A.; Rosen, B. A.; Baskin, A.; Repnin, N.; Pisasale, D.; Phillips, P.; Zhu, W.; Haasch, R.; Klie, R. F.; Kral, P.; Abiade, J.; Salehi-Khojin, A. *Nat. Commun.* **2014**, *5*, 4470.

(9) Hori, Y.; Takahashi, R.; Yoshinami, Y.; Murata, A. *J. Phys. Chem. B* **1997**, *101*, 7075.

(10) Schouten, K. J. P.; Qin, Z. S.; Gallent, E. P.; Koper, M. T. M. *J. Am. Chem. Soc.* **2012**, *134*, 9864.

(11) Li, C. W.; Ciston, J.; Kanan, M. W. *Nature* **2014**, *508*, 504.

(12) Fu, S. S.; Somorjai, G. A. *Surf. Sci.* **1992**, *262*, 68.

(13) Sandoval, M. J.; Bell, A. T. *J. Catal.* **1993**, *144*, 227.

(14) Perez-Alonso, F. J.; McCarthy, D. N.; Nierhoff, A.; Hernandez-Fernandez, P.; Strebel, C.; Stephens, I. E. L.; Nielsen, J. H.; Chorkendorff, I. *Angew. Chem., Int. Ed.* **2012**, *51*, 4641.

(15) van der Niet, M. J. T. C.; den Dunnen, A.; Juurlink, L. B. F.; Koper, M. T. M. *Angew. Chem., Int. Ed.* **2010**, *49*, 6572.

(16) Johansson, T. P.; Ulrikkeholm, E. T.; Hernandez-Fernandez, P.; Escudero-Escribano, M.; Malacrida, P.; Stephens, I. E. L.; Chorkendorff, I. *Phys. Chem. Chem. Phys.* **2014**, *16*, 13718.

(17) LaGrange, T.; Reed, B. W.; Wall, M.; Mason, J.; Barbee, T.; Kumar, M. *Appl. Phys. Lett.* 2013, *102*01190510.1063/1.4772589.

(18) Rauch, E. F.; Veron, M.; Portillo, J.; Bultreys, D.; Maniette, Y.; Nicolopoulos, S. *Microscopy and Analysis* **2008**, *22*, S5.

(19) *IUPAC Solubility Data Series*; Cargill, R. W., Ed.; Pergamon Press: Oxford, 1990; Vol. *43*.

(20) Nerlov, J.; Sckerl, S.; Wambach, J.; Chorkendorff, I. *Appl. Catal., A* **2000**, *191*, 97.

(21) Vollmer, S.; Witte, G.; Woll, C. *Catal. Lett.* **2001**, *77*, 97.

(22) Makino, T.; Okada, M. *Surf. Sci.* **2014**, *628*, 36.

(23) Strunk, J.; d'Alnoncourt, R. N.; Bergmann, M.; Litvinov, S.; Xia, X.; Hinrichsen, O.; Muhler, M. *Phys. Chem. Chem. Phys.* **2006**, *8*, 1556.

(24) d'Alnoncourt, R. N.; Bergmann, M.; Strunk, J.; Loffler, E.; Hinrichsen, O.; Muhler, M. *Thermochim. Acta* **2005**, *434*, 132.

(25) Montoya, J. H.; Shi, C.; Chan, K.; Nørskov, J. K. *J. Phys. Chem. Lett.* **2015**, *6*, 2032.

(26) Calle-Vallejo, F.; Koper, M. T. M. *Angew. Chem., Int. Ed.* **2013**, *52*, 7282.

(27) Stukowski, A.; Markmann, J.; Weissmuller, J.; Albe, K. *Acta Mater.* **2009**, *57*, 1648.

DOI: 10.1021/jacs.5b06227
J. Am. Chem. Soc. 2015, 137, 9808−9811